Development of Inverse-Opal-Structured Charge-Deficient Co_9S_8@nitrogen-Doped-Carbon to Catalytically Enable High Energy and High Power for the Two-Electron Transfer I^+/I^- Electrode

Hu, Tao; Zhao, Yuanyuan; Yang, Yihan; Lv, Haiming; Zhong, Rong; Ding, Feng; Mo, Funian; Hu, Haibo; Zhi, Chunyi; Liang, Guojin

Published in:
Advanced Materials

Published: 02/05/2024

Document Version:
Final Published version, also known as Publisher's PDF, Publisher's Final version or Version of Record

Published version (DOI):
10.1002/adma.202312246

Publication details:
Hu, T., Zhao, Y., Yang, Y., Lv, H., Zhong, R., Ding, F., Mo, F., Hu, H., Zhi, C., & Liang, G. (2024). Development of Inverse-Opal-Structured Charge-Deficient Co_9S_8@nitrogen-Doped-Carbon to Catalytically Enable High Energy and High Power for the Two-Electron Transfer I^+/I^- Electrode. *Advanced Materials*, *36*(18), Article 2312246. https://doi.org/10.1002/adma.202312246

ADVANCED MATERIALS
www.advmat.de

Development of Inverse-Opal-Structured Charge-Deficient Co_9S_8@nitrogen-Doped-Carbon to Catalytically Enable High Energy and High Power for the Two-Electron Transfer I^+/I^- Electrode

Tao Hu, Yuanyuan Zhao, Yihan Yang, Haiming Lv, Rong Zhong, Feng Ding, Funian Mo, Haibo Hu,* Chunyi Zhi,* and Guojin Liang**

The iodine (I) electrode involving two-electron transfer chemistry by converting between I^+ and I^-, has the potential to deliver theoretically doubled capacity and higher working voltage platforms, thus achieving higher energy density. However, owing to the slow kinetics of the cascade two-electron transfer reactions, the system suffers from large overpotentials and low power density, especially at high working currents and low temperatures. Here, an inverse-opal-structured cobalt sulfide@nitrogen–doped-carbon (Co_9S_8@NC) catalyst with unique charge-deficient states is developed to promote the reaction kinetics of the I^-/I^+ electrode. The charge-deficient Co_9S_8@NC catalyst not only enables strong physicochemical adsorption with the iodine species but also significantly reduces the activation energy and interfacial charge transfer resistance of the cascade $I^+/I^0/I^-$ conversion reaction. Consequently, the prototypical Zn‖$I^+/I^0/I^-$ battery equipped with the Co_9S_8@NC catalyst can deliver a high energy density of 554 Wh kg^{-1} and a stable cycle life of 5000 cycles at 30 °C. Moreover, at a subzero temperature of −30 °C, the battery can exhibit enhanced kinetics and a high power density of 1514 W kg^{-1}, high energy density of 485 Wh kg^{-1}.

1. Introduction

Compared to the generally employed insertion/extraction type electrode in aqueous zinc-iodine battery systems,[1,2] the conversion-type iodine (I) electrode has garnered significant attention as a promising cathode candidate,[3] owing to its relatively high theoretical specific capacity and excellent redox reversibility.[4] Generally, the single-electron transfer I^0/I^- reaction is employed as the cathode reaction,[5] providing a theoretical specific capacity of 211 mAh g^{-1}. Recently, a two-electron transfer electrode, termed as the $I^+/I^0/I^-$ electrode, has been investigated and found to offer significantly improved capacity and distinct higher working voltage platforms, thus ensuring higher energy density.[4,6] Specifically, concentrated chloride ions (Cl^-) were introduced into the electrolyte to stabilize I^+, enabling the formation of the

T. Hu, H. Hu
School of Materials Science and Engineering
Anhui University
Hefei 230601, China
E-mail: haibohu@ahu.edu.cn

T. Hu, Y. Zhao, F. Ding, G. Liang
Institute of Technology for Carbon Neutrality
Shenzhen Institute of Advanced Technology
Chinese Academy of Sciences (CAS)
Shenzhen, Guangdong 518055, China
E-mail: gj.liang@siat.ac.cn

Y. Zhao
Key Laboratory of Materials Modification by Laser
Ion and Electron Beams (Dalian University of Technology)
Ministry of Education
Dalian 116024, China

Y. Yang, H. Lv
Songshan Lake Materials Laboratory
Dongguan, Guangdong 523808, China

R. Zhong, C. Zhi
Department of Materials Science and Engineering
City University of Hong Kong
83 Tat Chee Avenue, Kowloon, Hong Kong SAR 999077, China
E-mail: cy.zhi@cityu.edu.hk

F. Mo
School of Materials Science and Engineering
Harbin Institute of Technology
Shenzhen 518055, China
E-mail: mofunian@hit.edu.cn

The ORCID identification number(s) for the author(s) of this article can be found under https://doi.org/10.1002/adma.202312246

DOI: 10.1002/adma.202312246

interhalogen ICl as the final charged product at the cathode side.[4,7] This pioneering approach offered a high specific capacity of 594 mAh g^{-1} with two distinct voltage platforms of 1.83 and 1.29 V, resulting in 276% improvement in the energy density of 750 Wh kg^{-1} compared to the theoretical energy density (272 Wh kg^{-1}) of the traditional I^0/I^- electrode.[4] Ti_3C_2-based MXene has also been utilized as a host for the two-electron transfer ICl electrode at the interlayer space, further increasing the energy density by 231% compared to that of the I^0/I^- electrode.[6] These remarkable improvements render the two-electron transfer $I^+/I^0/I^-$ electrode as a competitive high-energy electrode candidate for zinc-based batteries.

Despite the improved energy density, the working currents and corresponding power of the $I^+/I^0/I^-$ electrode remained relatively low,[3,6] typically below 3 A g^{-1}. Consequently, these results in enlarged overpotentials and lower capacities, especially at high working currents.[8] Moreover, at lower temperatures, the kinetics of the cascade conversion reaction tend to deteriorate further, aggravating voltage polarization and subsequent capacity and power degradation of the $I^+/I^0/I^-$ electrode.[9]

Introducing catalysts is an effective strategy for enhancing the kinetics of the conversion reaction and the overall electrochemical performance,[7,10] using electrodes such as the chalcogen and halogen conversion electrodes based on either single or multiple-electron transfer reactions.[11,12] Previous studies have focused on improving the kinetics of the conversion reaction for the single-electron transfer I^0/I^- electrode.[12,13] For example, Fe loaded onto nitrogen-doped-carbon (NC) as Fe-NC catalysts have been successfully developed to catalytically enhance the kinetics and reversibility of the single-electron iodine electrode, reducing the reaction energy barrier through the physicochemical confinement effect and significantly improving energy and power performance.[11] Moreover, graphitic N in NC catalysts exhibits strong catalytic activity, enabling the direct I^0/I^- conversion and inhibiting the formation of triiodide (I_3^-) by reducing the dissociation energy barrier.[12,14] This not only enhance the power performance but also increases the cycling stability of the I^0/I^- electrode in single-electron transfer processes.[12] However, few improving strategies have been reported for improving the kinetic regulations of the cascade reaction of the two-electron transfer process for the high-energy $I^+/I^0/I^-$ electrode, where the corresponding energy and power could be further enhanced.

Here, we introduced an effective catalyst to enhance the reaction kinetics of the cascade $I^+/I^0/I^-$ conversion electrode, thus achieving higher energy and power performance.[15] Specifically, a highly efficient catalyst, Co_9S_8@NC, was developed, in which the Co_9S_8 nanoparticles were monodispersed and uniformly embedded within the porous honeycomb and interconnected NC framework, forming a core–shell structure.[16] The monodispersed Co_9S_8 nanoparticles were featured with charge-deficient states,[17] enabling strong electrostatic attraction toward the active iodine species. Additionally, Co_9S_8@NC could significantly reduce the energy barriers for the $I^+/I^0/I^-$ conversion reaction and accelerate the interfacial ion-transfer kinetics, resulting in improved reaction kinetics with superior energy and power density.[18] Even at a low temperature of −30 °C, high energy and high power, along with long cycling stability, could be successfully achieved for the two-electron transfer Zn‖$I^+/I^0/I^-$ battery. The pioneering attempts in our work can provide new avenues toward achieving highly improved performance originating from the iodine-based electrode chemistry.[19]

2. Results and Discussion

2.1. Characterization of the Co_9S_8@NC Catalyst

X-ray diffraction (XRD) was used to examine the crystalline phase of the synthesized samples. The XRD peaks could be assigned to crystalline Co_9S_8 (JCPSD NO.65-6801). **Figure 1a** shows the individual peaks of Co_9S_8. The peak at 19.8° can be attributed to the host NC framework of the Co_9S_8 nanoparticles. Raman spectra exhibited a peak at 670 cm^{-1}, which could be attributed to Co_9S_8, and suggested a larger I_D/I_G ratio of 1.18 for Co_9S_8@NC, with more defect/edge sites compared to that in the NC framework,[20,21] where the I_D and I_G represent the intensity of D and G bands of the typical NC framework (Figure S1, Supporting Information). The Brunauer–Emmett–Teller (BET) isotherm of nitrogen adsorption–desorption exhibited an evident hysteresis loop and an ultrahigh specific surface area of 535.3 m^2 g^{-1} (Figure 1b). Both mesopores and macropores coexisted (Figure S2, Supporting Information), with the pore size centered at 15 and 200 nm, respectively (inset of Figure 1b). These mesoporous and macroporous features in the NC framework originated from the etched silicon spheres during the catalyst preparation process (details in the Experimental Section[16]). Such a configuration was conducive to exposing more active sites and facilitating faster mass transfer at the catalyst/electrolyte interface.

Moreover, a comparative study were conducted on the physicochemical properties of Co_9S_8@NC and the NC frameworks. X-ray photoelectron spectroscopy (XPS) was employed to characterize the chemical composition and bonding structure. In the Co_9S_8@NC catalyst, the Co $2p_{3/2}$ peak shifted to a higher binding energy of 780.5 eV compared to the general valence band of 778.3 eV for Co in the Co_9S_8 nanoparticles, while the binding energy at 163.5 and 164.6 eV, respectively, assigned to the S $2p_{3/2}$ and S $2p_{1/2}$ also shifted to higher binding energy states compared with 162.4 eV of S $2p_{1/2}$ and 161.4 eV of $2p_{3/2}$ in general Co_9S_8 (Figure 1c; and Figure S3, Supporting Information).[22,23] The shift to the higher valence states for Co and S could be attributed to the electron transport from Co_9S_8 to the NC framework. Meanwhile, the valence state of N in Co_9S_8@NC appeared at 399.08 eV, which is lower compared to the value of 400.08 eV for the bare NC framework (Figure 1c; and Figure S4, Supporting Information). This difference could originate the electron transferred from Co_9S_8 to the NC framework. Taken together, Co elements in Co_9S_8@NC were in a charge-deficient state, which could serve as the effective adsorption sites for the electron-sufficient iodine species, e.g., I_2 and I_3^-. On the other side, the work functions of the Co_9S_8@NC and the NC framework were measured by ultraviolet photoelectron spectroscopy (UPS[24]). The work functions of Co_9S_8@NC and the NC were 5.32 and 7.67 eV, respectively (Figures S5 and S6, Supporting Information). The difference in work functions between Co_9S_8@NC and NC could be correlated to less energy of Co_9S_8@NC to activate electrons to reach the Fermi level,[25] (Figure 1d), which

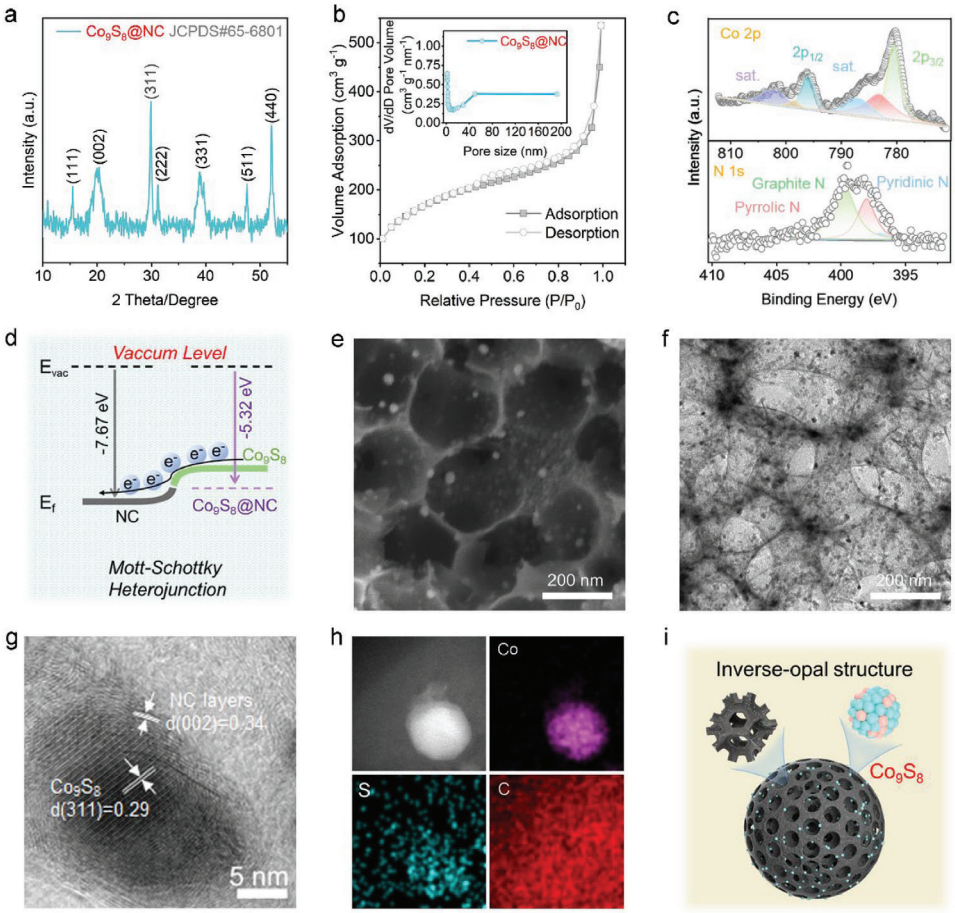

Figure 1. Structural elucidation and fundamental characterization of catalysts. a) XRD profile of Co_9S_8@NC. b) N_2 adsorptiom–desorption isotherms of Co_9S_8@NC and the inset is the corresponding pore-size distribution. c) High-resolution XPS spectra of the Co 2p and N 1s inCo_9S_8@NC. d) Diagram of work function of Co_9S_8@NC corresponding to the UPS results. e,f) SEM image and TEM image of the monodispersed Co_9S_8 onto the porous NC framework. g) The HRTEM image of Co_9S_8@NC with core–shell configuration. h) Corresponding EDX mapping of Co, S, C. i) Structural model diagram of the inverse-opal-structured catalyst.

originated from the spontaneous electron transfer from Co_9S_8 to the NC framework and the built-up electric field at the charge-deficient interface. This self-driven charge redistribution is known as the Mott–Schottky effect, creating charge-deficient sites in Co_9S_8 to serve as effective adsorption sites for iodine species.

The scanning electron microscopy (SEM) image of Co_9S_8@NC (Figure 1e) indicated a porous, inverse-opal structure, with the interconnected macropores containing a highly conductive NC framework and the monodisperse Co_9S_8 nanoparticles with a diameter of ≈10 nm. Notably, the internal honeycomb pores were interconnected to facilitate electrolyte infiltration and ion transport. This honeycomb structure was obtained by combining in situ silica etching and mild chemical reactions during catalyst preparation. The morphology of the silica spheres and the synthetic protocol of Co_9S_8@NC are shown in Figures S7 and S8 (Supporting Information). The control sample—the bare NC framework—also exhibited an identical honeycomb NC framework but without the Co_9S_8 nanoparticles (Figure S9, Supporting Information). The inverse opal-structure of the Co_9S_8@NC composite was further investigated by high-resolution transmission electron microscopy (HRTEM), which revealed a unique honeycomb porous structure comprising an interconnected NC skeleton and monodispersed Co_9S_8 nanoparticles (Figure 1f; and Figure S9, Supporting Information). The lattice distance in the crystal was measured to be 0.29 nm and could be assigned to the (311) plane of Co_9S_8. The NC layer encapsulated the outermost layer of the Co_9S_8 nanoparticles, generating a core–shell structure (Figure 1g). The uniformly monodispersed Co_9S_8 nanoparticles, rather than agglomerated particles, were essential to increase the number of active adsorption sites and enhance the catalytic activity of the iodine redox reactions. Elemental mapping analysis further confirmed the size and elemental composition of Co_9S_8@NC (Figure 1h). HRTEM images and the corresponding EDX elemental images confirmed a consistent distribution of Co, S, and C. Collectively, these structural analyses unequivocally verified the formation of the Co_9S_8-NC core–shell structure. The inverse opal-structured Co_9S_8@NC model diagram and its locally enlarged diagram (Figure 1i) demonstrate the mono dispersion of the Co_9S_8 nanoparticles and the internal honeycomb porous structure.

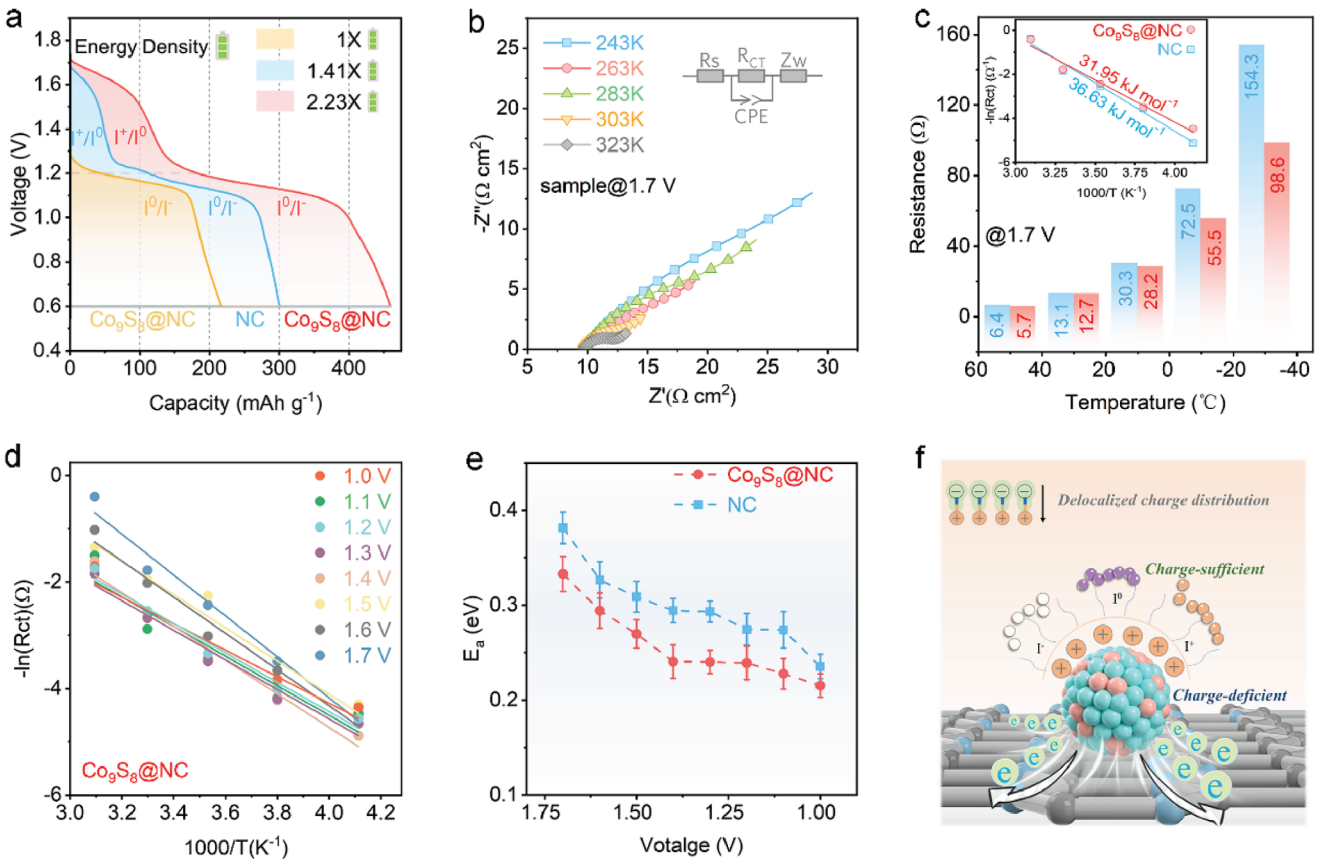

Figure 2. The variations of activation energy during the $I^+/I^0/I^-$ conversion reactions. a) The discharge curve of $I^+/I^0/I^-$ reaction and I^0/I^- reaction based on Co_9S_8@NC electrode and NC electrode, respectively. The battery symbol represents the delivered energy density based on the I^0/I^- reaction with single electron transfer. b) EIS results at different temperatures at the charged state of 1.7 V. The inset is the equivalent circuit where the R_S is the intrinsic ohmic resistance, R_{CT} is the charge transfer resistance, Z_W is the ion diffusion resistance, CPE is the capacitance contributed by the charge transfer process. c) The R_{CT} of Co_9S_8@NC electrode and NC electrode at different temperatures at 1.7 V. The inset is Arrhenius profile showing the linear relationship between the logarithm of the charge transfer resistance and the inverse of the absolute temperature at 1.7 V. d) The linear relationship between the logarithm of the charge transfer resistance and the inverse of the absolute temperature at the voltage range from 1 to 1.7 V. e) The variations in activation energy at 1–1.7 V. f) The scheme of interacting manners between the active iodine species and the Co_9S_8@NC.

2.2. Catalyzed $I^+/I^0/I^-$ Reaction

Afterward, the electrochemical performance was examined to investigate the catalytic activity of Co_9S_8@NC on the $I^+/I^0/I^-$ reaction, while the contrast NC samples were tested under identical operating conditions. According to the galvanostatic charge–discharge (GCD) profiles, the $I^+/I^0/I^-$ reaction based on the Co_9S_8@NC electrode could not only deliver a high specific capacity of 458 mAh g^{-1} compared to the 301 mAh g^{-1} of the NC electrode (the calculation based on the output capacity of the whole electrode and the mass of iodine unless otherwise specified) but also two distinct higher discharging voltage platforms of the Co_9S_8@NC electrode than those of the NC electrode (**Figure 2a**; and Figure S10, Supporting Information), where the detailed values of the GCD profiles are exhibited in Table S1 (Supporting Information). Moreover, the two-electron transfer $I^+/I^0/I^-$ reaction based on the Co_9S_8@NC electrode accommodated larger energy density with notably higher capacity and voltage compared to the generally applied single-electron transfer I^0/I^- reaction of 214 mAh g^{-1} (Figure 2a).

Subsequently, the catalytic activities of the Co_9S_8@NC electrode and the NC electrode were evaluated by performing the electrochemical impedance spectroscopy (EIS) at different working potentials and temperatures (Figure 2b; and Figures S11 and S12, Supporting Information). EIS results can provide valuable insights into the interfacial transfer resistances of the conversion iodine electrode and the corresponding reaction kinetics. The fitted values of the charge transfer resistance (R_{CT}) and the solution resistance (R_S) are summarized in Table S2 (Supporting Information) for the Co_9S_8@NC electrode and in Table S3 (Supporting Information) for the NC electrode. The charge transfer resistances of the Co_9S_8@NC electrode were notably smaller than those of the NC electrode at different temperatures, as shown in Figure 2c; and Figure S13 (Supporting Information). By analyzing the linear relationship between the charge transfer resistance and the different absolute temperatures using the formula provided in Note S1 (Supporting Information), the activation energy of the Co_9S_8@NC electrode was lower as 31.95 kJ mol^{-1} compared to 36.63 kJ mol^{-1} of the NC electrode at the identical charged state of 1.7 V (inset of Figure 2c). Additionally,

the charge transfer resistances at different discharged voltage range from 1.7 to 1 V and temperature ranges from 243 to 323 K were fitted into a linear relationship following the Arrhenius relation (Figure 2d; and Figure S14, Supporting Information). The Co_9S_8@NC electrode was featured with lower E_a compared to the NC electrode throughout the discharging process at all the voltage and temperature conditions (Figure 2e; and Table S4, Supporting Information), which could be originated from the enhanced reaction kinetics of the Co_9S_8@NC electrode to accelerate the charge transfer process of the $I^+/I^0/I^-$ reaction. Based on the structural and electrochemical analyses, a diagram on the working and catalytic function of Co_9S_8@NC is shown in Figure 2f. At the Co_9S_8@NC interface with delocalized charge distribution, charge-deficient sites were configured at the Co_9S_8 to form strong adsorption interaction with the electron-sufficient iodine species, e.g., I^-, I^0, and I^+, and promote the charge transfer process and redox process with reduced energy barriers.

2.3. Electrochemical Performance of the Co_9S_8@NC Electrode Working Based on the $I^+/I^0/I^-$ Reaction

Cyclic voltammetry (CV) curves of the Co_9S_8@NC and NC electrodes were collected to further study the catalytic kinetic performance on the $I^+/I^0/I^-$ reaction; two coupled redox peaks based on a two-electron transfer reaction (**Figure 3a**) were observed. Specifically, the Co_9S_8@NC electrode exhibited a relatively larger response current than the NC electrode at a scan rate of 0.1 mV s^{-1}, which could be attributed to the improved reaction kinetics of the cascade reactions upon utilizing the Co_9S_8@NC electrode. Additionally, the peak current density (i_p) as a function of the square root of the scan rate ($v^{1/2}$) for the anodic and cathodic reactions was derived from the CV curves of the two electrodes at different scan rates (Figure 3b; and Figures S15 and S16, Supporting Information). The slopes of the reduction and oxidation processes for the Co_9S_8@NC sample were −7.14 and 5.10, respectively, which were higher than those of the NC electrodes (−2.61 and 2.41, respectively). This indicated that the reduction and oxidation reactions of the I species are diffusion-controlled by mass transport.[26] On the other side, the Tafel slopes derived from the LSV curves (Figure S17, Supporting Information) also revealed that the I^+/I^0 and I^0/I^- conversion reactions based on the Co_9S_8@NC electrode had smaller slopes than those of the NC electrode (Figure 3c). The smaller Tafel slopes corresponded to a sharp increase in the response current of the Co_9S_8@NC electrode. The above results demonstrate that the rapid electrocatalytic kinetics based on the Co_9S_8@NC electrode were more significant than those based on the NC electrode.

To analyze the interfacial charge transfer processes at different discharge states, in situ EIS was measured to evaluate the resistance variations during the redox process of the Co_9S_8@NC electrode at room temperature (30 °C) and low temperature (−30 °C) (Figure 3d,e; and Figure S18, Supporting Information), respectively, where the charge transfer was much smaller than the NC electrode. To gain deeper insights into interfacial charge transfer kinetics, the distribution relaxation time (DRT)[27–29] was subsequently analyzed by deconvoluting the EIS data. Specifically, the DRT spectrum could be deconvoluted into two peaks, denoted as P1 and P2, where P1 could be assigned to the electron transfer of the redox species, and P2 could correspond to the interface charge exchange and electrolyte mass transfer process (Note S2, Supporting Information). It was found that both P1 and P2 of the Co_9S_8@NC electrode shifted toward a lower time scale, where the corresponding peak width of P1 and P2 were relatively smaller and centered at the time scale range of 10^{-2}–10^{-1} s, verifying the faster redox reaction and the interface charge exchange kinetics of the Co_9S_8@NC electrode compared with the NC electrode (Figure 3f). In addition, even at a low temperature of −30 °C, the DRT results revealed that the Co_9S_8@NC electrode also exhibited faster kinetic mass transfer processes without significant degradation (Figure 3g). This can be attributed to the charge-deficient Co_9S_8@NC could promote interfacial charge transfer kinetics with rapid ion exchange and electron transport. A comparison between the constant current intermittent titration (GITT) profiles of Co_9S_8@NC and NC reveals that the Co9S8@NC electrode would accommodate smaller overvoltage compared to that of the NC electrode (Figure S19, Supporting Information), indicating the faster reaction kinetics of the Co_9S_8@NC electrode.

2.4. Working Mechanism of the Co_9S_8@NC Electrode

To elucidate the two-electron reaction mechanism, in situ Raman spectroscopy was employed to investigate the charged and discharged products, as shown in **Figure 4a**. An intrinsic I^- peak at 105 cm^{-1} was observed at the initial state. The I_3^- peak at 174 cm^{-1} gradually appeared and intensified along charging to 1.25 V throughout the first charging plateau. Moreover, the ICl peak centered at 203 cm^{-1} appeared once charged to 1.6 V and became prominent once charged to 1.7 V, while I^- was barely detected.[7,30] It indicated the full conversion from I^- to I^+ to complete the two-electron transfer reactions. Regarding the discharging process, the signal reversed with Icl disappeared and I^- reappeared, demonstrating the high reversibility of the conversion $I^+/I^0/I^-$ electrode.

To gain insight into the interacting manners of Co_9S_8@NC and NC with the active iodine species of the conversion reaction, i.e., the Icl, I_2, I_3^-, and I^-, density functional theory (DFT) calculations were performed. The differential charge densities and the optimized adsorption configurations of the different iodine species on the Co_9S_8@NC and pure NC electrode (Figure 4b,c) suggested that the charge was redistributed by transferring electrons from iodine to the Co_9S_8@NC electrode after iodine adsorption. For the NC electrode, the iodine species could also adsorb onto the NC electrode with charge redistribution (Figure S20, Supporting Information), where the adsorption configurations of the iodine species on the comparative NC electrode were evaluated to adsorb at the graphitic N, pyridinic N, and pyrrolic N sites, respectively (Figures S21 and S23, Supporting Information). The significant charge delocalization degree between the iodine species and the Co_9S_8@NC electrode is much larger compared to that of the NC electrode. It could be attributed to the strong adsorption of the charge-deficient Co_9S_8 sites with the iodine species. To resolve this, the adsorption energies for the involved iodine species as ICl, I_2, I_3^-, and ZnI_2 on Co_9S_8@NC are calculated with lower energy compared with those of NC (Figure 4d; and Note S3, Supporting Information), where the specific values of the adsorption energy were presented in Tables

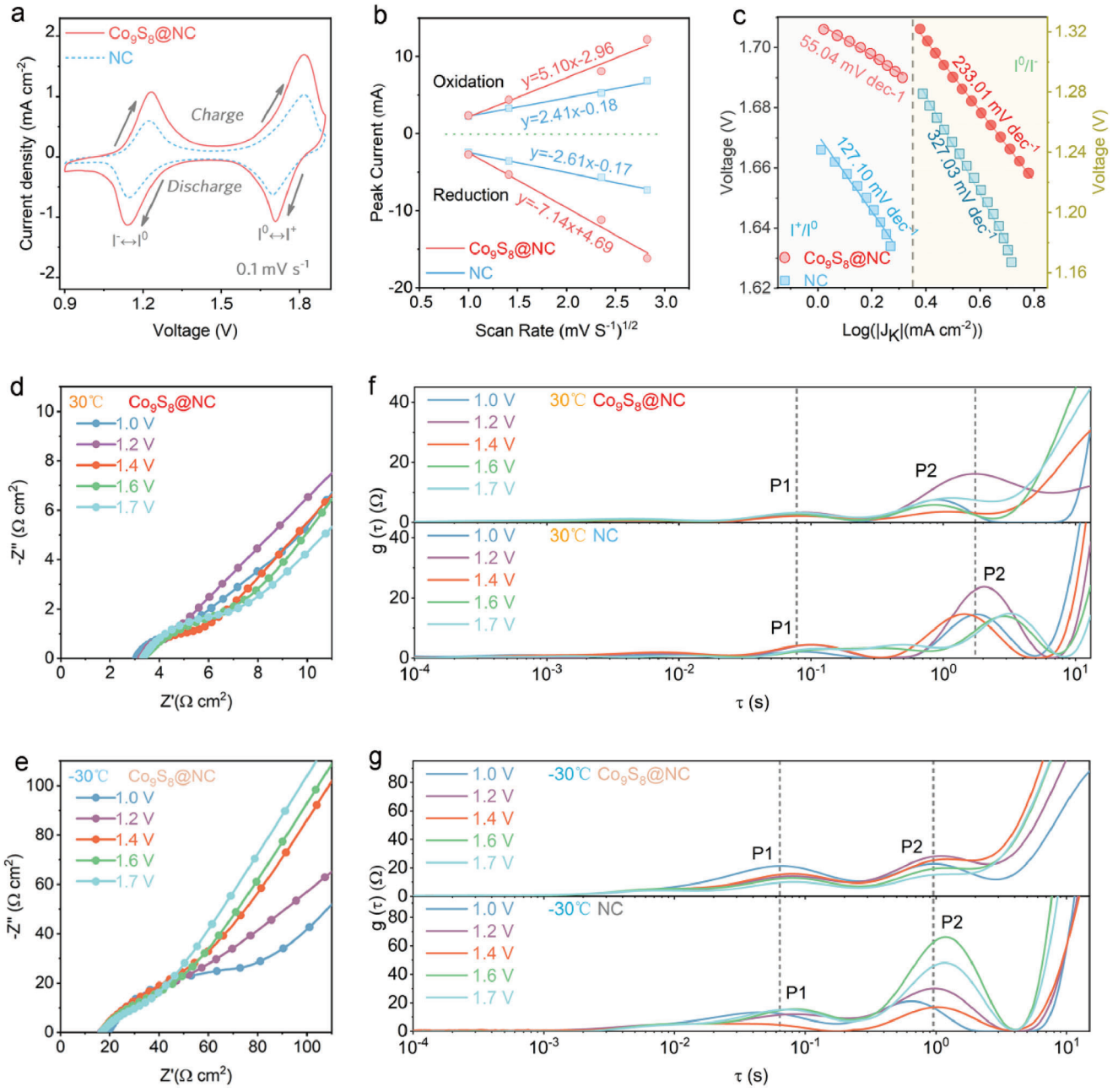

Figure 3. Electrochemical performance and kinetic analysis of Co_9S_8@NC electrode at different working voltage states and temperatures. a) CV profiles of Co_9S_8@NC electrode and NC electrode at 0.1 mV s^{-1}. b) Square root relationship between peak current and scan rate during CV conversion at 1–8 mV s^{-1}. c) The Tafel slopes of I^+/I^0 and I^0/I^- derived by LSV. d,e) In situ EIS results at room temperature 30 °C and low temperature −30 °C. f,g) The corresponding DRT results of Co_9S_8@NC electrode and NC electrode.

S5 and S6 (Supporting Information). The more negative adsorption energies based on the Co_9S_8@NC electrode could be correlated to more thermodynamically stable adsorption configurations, where the charge-deficient Co_9S_8@NC could indicate more electron transferred from the iodine species and promote strong adsorption with the Co_9S_8@NC electrode.

To understand the catalytic behaviors of Co_9S_8@NC for the iodine redox process, the Gibbs free energy of the ICl reduction pathways with the reaction intermediates was calculated in Figure 4e. The negative Gibbs free energy of Co_9S_8@NC indicated that the reduction process from ICl to ZnI_2 was exothermic and could occur spontaneously. When considering larger ΔG differences, it is indisputable that the reaction tends to become more spontaneous for the reduction process by converting from ICl to I_2. However, in the reverse oxidation process from I_2 to ICl, the considerable ΔG difference could hinder the reaction, making it the determining step for the whole oxidation process.[11] More specifically, the free energy for

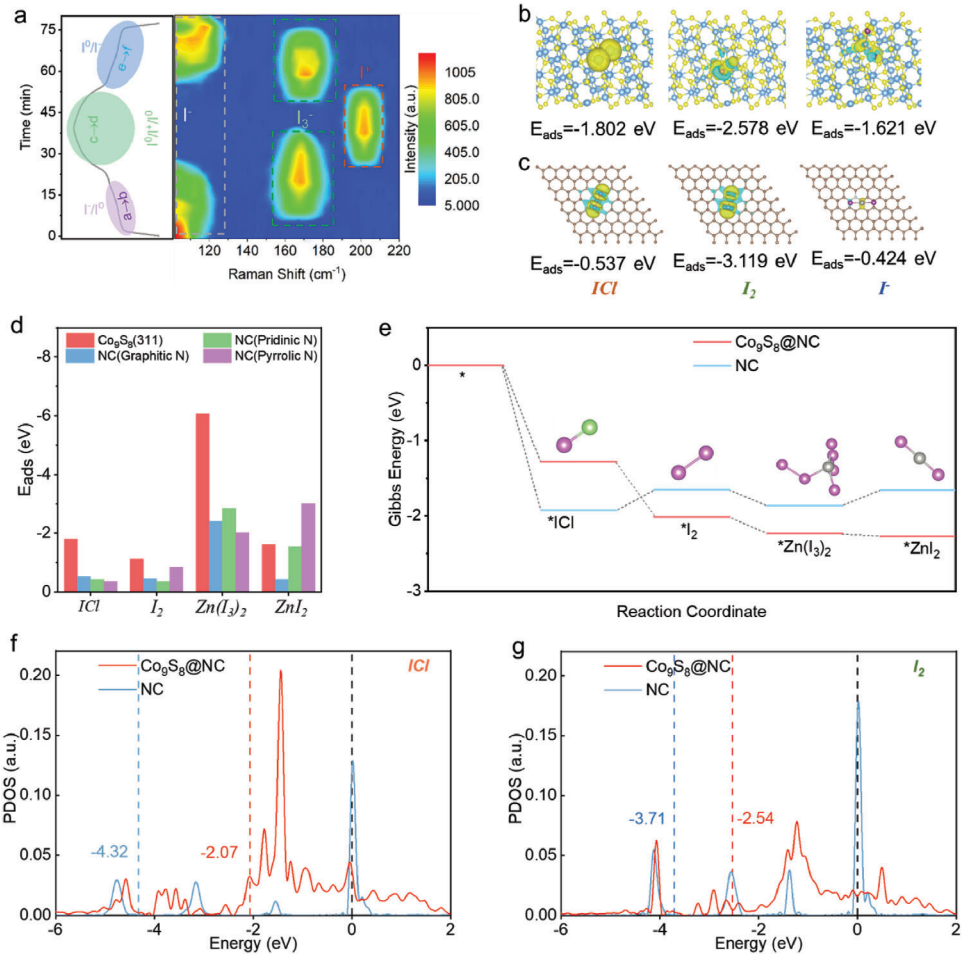

Figure 4. Catalytic analysis on the working mechanism of Co_9S_8@NC electrode. a) In situ Raman characterizations on the iodine intermediates during charging and discharging. b) The differential charge density of iodine and intermediates adsorbed on to Co_9S_8@NC and c) the NC electrode. d) The adsorption energy of different iodine species on Co_9S_8@NC and NC. e) The Gibbs free energy ladder diagram. f,g) The PDOS of ICl and I_2 on Co_9S_8@NC electrode and NC electrode, respectively. The blue, red, and black dashed lines correspond to the position of the p-band center, d-band center, and Fermi level, respectively.

the reduction process of the adsorbing iodine intermediates at the Co_9S_8@NC electrode were negative, viz., −1.277, −2.010, −2.234, and −2.267, respectively, which were energetically favorable for the whole iodine redox reaction. On the other side, regarding the NC electrode, the free energy was −1.918, −1.648, −1.862, and −1.653, respectively, with the positive ΔG as 0.27 eV for the conversion from ICl to I_2 and 0.209 eV from $Zn(I_3)_2$ to ZnI_2 (Figure 4e). Taken together, the calculational results were consistent with the above experimental results, and the reaction kinetics from ICl→ZnI_2 was largely promoted based on the Co_9S_8@NC electrode, which could be attributed to its charge-deficient states and unique honeycomb porous structure.

Moreover, the projected density of states (PDOS) of the dominant iodine intermediates as ICl and I_2 were further calculated to evaluate the interaction between the iodine and the catalytic electrode. Compared with the relatively isolated mode of pure I_2 and ICl (Figure S24, Supporting Information), the PDOS modes of ICl/Co_9S_8@NC, ICl/NC, I_2/Co_9S_8@NC, and I_2/NC have presented continuous mode with considerable distributions around the Fermi level, which was originated from the orbital hybridization of iodine with the hosting electrode. In addition, the d-band centers of ICl and I_2 for the Co_9S_8@NC electrode were −2.07 and −2.54 eV, respectively, showing a shift toward the Fermi level compared to −4.32 and −3.71 eV of the contrast NC electrode (Figure 4f). thereby indicating a more minor energy barrier for electron transfer[11] (Figure 4g). It should be noted that it is generally accepted that the d-band center serves as an effective descriptor of adsorption energy,[31] where the projected density of states (PDOS) reveals a closer position of the d-band center to the Fermi level of Co_9S_8@NC compared to the p-band center NC, indicating the enhanced adsorption interactions with iodine species (ICl, I_2). It is consistent with the calculated adsorption energies based on the Co_9S_8@NC electrode (Figure S20, Supporting Information). The d-p band center difference is recognized as a crucial descriptor predicting the electrocatalytic activity of metallic compounds. Valence electrons in transition metal compounds typically reside in the d-orbitals of metals and the p-orbitals of nonmetals. Bandgaps correlate with charge transfer energies, where lower

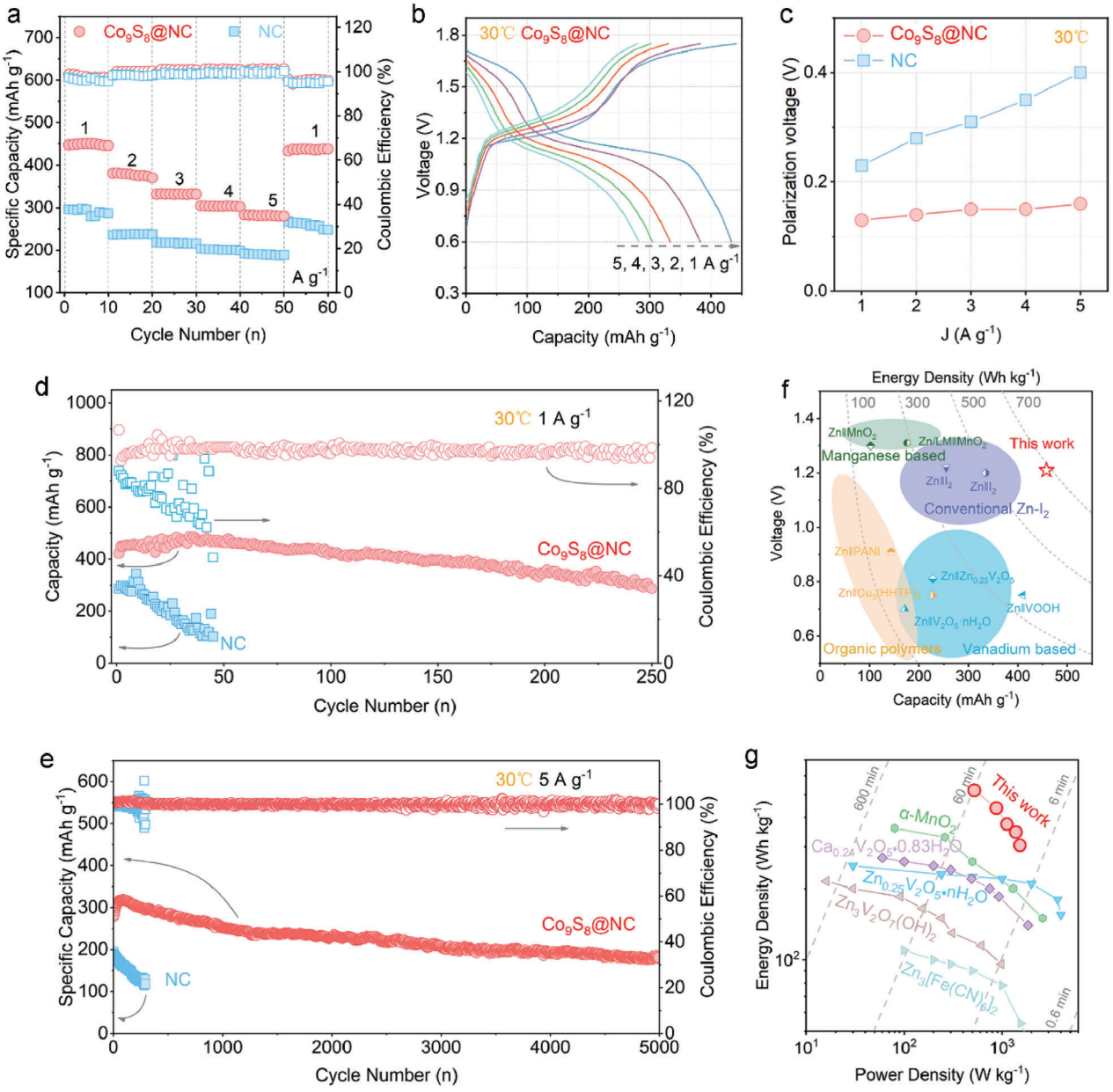

Figure 5. The Zn||I/Co_9S_8@NC battery performance at 30 °C. a) The rate performance at the different working currents from 1 to 5 A g^{-1}. b) The charge–discharge curves at different currents. c) Corresponding polarization voltages at different currents. d,e) Cycling performance at a low current of 1 A g^{-1} and high current of 5 A g^{-1}, respectively. f) Comparison of capacity and voltage of the electrode candidates with the reported electrode candidates in Zn-based batteries. g) The comparative Ragone plot of the energy density and the power density.

charge transfer energies may facilitate electron transfer and catalytic activity. The narrower bandgap of Co_9S_8 upon loading possibly enhances electron exchange, thus augmenting interfacial multivalent iodine redox kinetics. Correspondingly, the highest adsorption energy values for I^-, I_3^-, I_2, and ICl on Co_9S_8@NC, as depicted in Figure 4b,c, imply that Co_9S_8 nanoparticles serve as the catalytic active center. It is consistent with the experimental UPS and DRT results for the superior charge-transfer kinetics. Overall, the Co_9S_8@NC was an effective catalyst for the conversion reaction with enhanced charge transfer kinetics.

2.5. Battery Performance

The iodine electrode reaction based on the Co_9S_8@NC, that is, the I/Co_9S_8@NC electrode, was characterized in full battery configurations. First, the rate performance of the Zn||I/Co_9S_8@NC battery was evaluated with the specific currents ranging from 1 to 5 A g^{-1}, where Zn||I/Co_9S_8@NC exhibited higher reversible capacities of 458, 380, 333, 304, and 282 mAh g^{-1}, respectively. On the other side, the Zn||I/NC battery only exhibited reversible capacities of 298, 237, 218, 200, and 190 mAh g^{-1} at identical working currents (**Figure 5a**; and Figure S25, Supporting

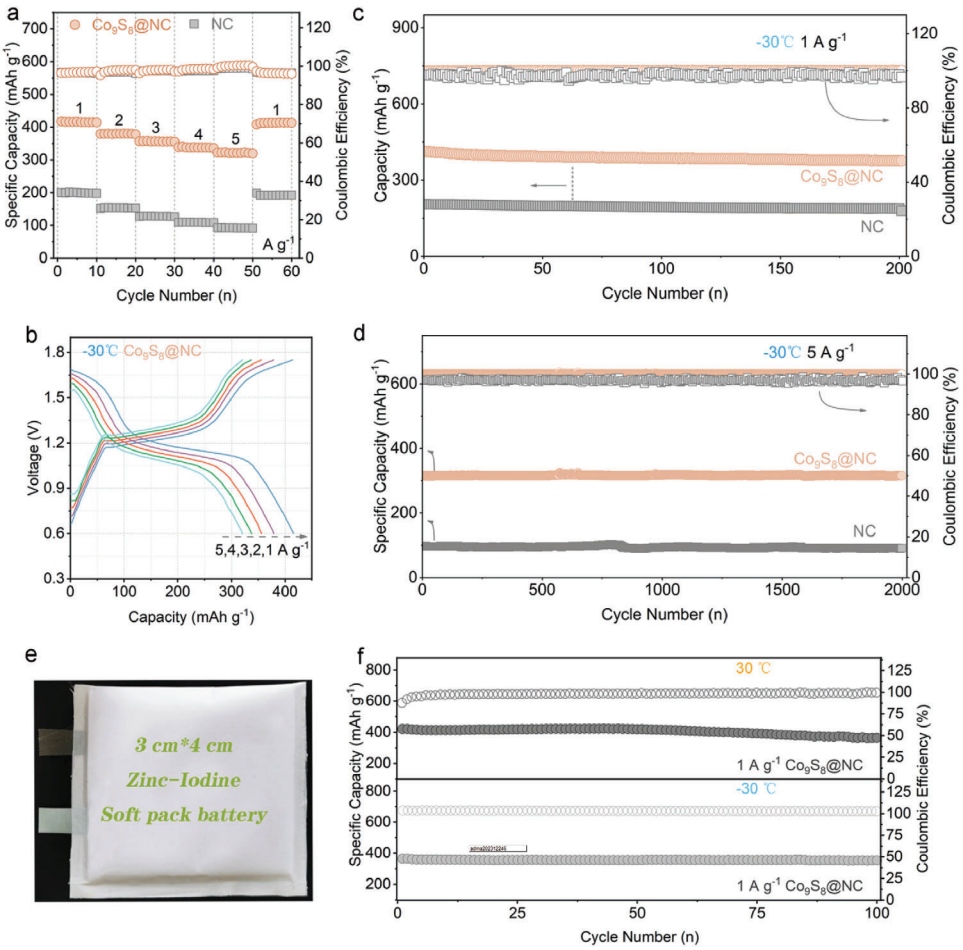

Figure 6. Battery performance of Zn||I/Co_9S_8@NC at low-temperature. a) Rate performance at different working currents at −30 °C. b) The charge–discharge curves of different currents. c,d) Cycling performance at a low current of 1 A g^{-1} and high current of 5 A g^{-1}, respectively. e) The picture of a 3 cm × 4 cm sized soft pack cell. f) Cyclic performance of the soft pack at low temperature and high temperature.

Information). It is worth mentioning that the theoretical capacity of the two-electron iodine conversion process is 422 mAh g^{-1}, but the Co_9S_8@NC could accommodate the capacity of 458 mAh g^{-1} due to the capacitive capacity contributed by the Co_9S_8@NC and NC electrode (Figure S26, Supporting Information).[11] The capacitive capacity based on the blank hosting materials, i.e., without iodine, was tested that the Co_9S_8@NC electrode could deliver 42.5 mAh at 1 A g^{-1} and 29.8 mAh g^{-1} at 5 A g^{-1} based on the electrode mass (Figure S27, Supporting Information). Specifically, the I/Co_9S_8@NC electrode demonstrated a significantly higher energy density of 554 Wh kg^{-1}, which was 158% higher compared to the 350 Wh kg^{-1} achieved with the I/NC electrode. Furthermore, the single-electron transfer I^0/I^- electrode could deliver a smaller energy density of 248 Wh kg^{-1} (Figure 2a). Thus, the energy density of the $I^+/I^0/I^-$ electrode was 223% higher than that of the I^0/I^- electrode, underscoring the superiority of utilizing the two-electron transfer reaction for the $I^+/I^0/I^-$ electrode. Moreover, the GCD profiles of the I/Co_9S_8@NC and the I/NC electrodes at 30 °C were exhibited in Figure 5b; and Figure S28 (Supporting Information), respectively. Apart from the larger capacity, the polarization voltage of Zn||I/Co_9S_8@NC battery was much lower than those of Zn||I/NC, especially at high working currents, e.g., 225 mV smaller of the polarization voltage Zn||I/Co_9S_8@NC at 5 A g^{-1} (Figure 5c). Even at a large current density of 5 A g^{-1}, the Zn||I/Co_9S_8@NC showed the reliability of a two-discharging platform, with an average reversible capacity of 282 mAh g^{-1}. It was consistent with the smaller interfacial charge transfer resistance of the I/Co_9S_8@NC electrode compared to the I/NC electrode (Figure 3f,g).

Furthermore, Zn||I/Co_9S_8@NC cell exhibited a decent long-term cycle performance at a current density of 1 A g^{-1} at 30 °C at room temperature, with a capacity retention of 63.21% after 250 cycles, and still maintained an ultra-high capacity of 286 mAh g^{-1} (Figure 5d). In comparison, the capacity of the comparison sample Zn||I/NC had decayed to 103 mAh g^{-1} at 48 cycles, and the capacity retention rate was only 34.56%. It should be emphasized that the Zn||I/Co_9S_8@NC cell was featured with more stable coulombic efficiency (CE) reaching 100% compared with the inferior CE of Zn||I/NC, which could be assigned to the strong adsorption energy between the active iodine and the hosting Co_9S_8@NC. Moreover, the Zn||I/Co_9S_8@NC could deliver long cycling stability with 60.11% capacity retention after 5000 cycles at 5 A g^{-1}, and an ultrahigh power density of 1526 W kg^{-1} (Figure 5e). In contrast, the capacity of the contrast Zn||I/NC

battery quickly decayed to 118 mAh g^{-1} after 292 cycles at 5 A g^{-1}. Due to the highly improved capacity and the discharge plateau, the Zn‖I/Co_9S_8@NC battery based on a two-electron transfer reaction exhibited performance superiority compared to the generally applied electrode materials for Zn-based batteries (Figure 5f; and Table S7, Supporting Information), such as the vanadium-based, manganese-based, and the Prussian-based electrode materials.[30,32–38] In addition, our system exhibits an outstanding energy density of 554 Wh kg^{-1} and power density of 1526 W kg^{-1}, which were superior among the reported aqueous zinc battery systems[30,32–34,36,37] (Figure 5g; and Table S8, Supporting Information). Moreover, the self-discharge performance was tested at full charge state for the Co_9S_8@NC and NC electrodes, respectively. Specifically, there was 86.9% capacity retention for the Co_9S_8@NC electrode after 24 h rest, while it was 74.6% for the NC electrode (Figure S29, Supporting Information). The higher capacity retention could be assigned to the strong electrostatic attraction between the Co_9S_8@NC and the active iodine species.

The Zn‖I/Co_9S_8@NC battery performance was characterized by low temperature at −30 °C. The rate performance was first tested at 1–5 A g^{-1}, and it was found that Zn‖I/Co_9S_8@NC exhibited high reversible capacity at low temperatures the reversible capacities are 417, 380, 357, 338, and 321 mAh g^{-1} at −30 °C, realized a high power density of 1514 W kg^{-1}, a high energy density of 485 Wh kg^{-1} (**Figure 6a**). According to the GCD profiles (Figure 6b; and Figure S30, Supporting Information), the polarization voltage of Zn‖I/Co_9S_8@NC is much lower than that of I/Zn‖NC, while the polarization voltage of Zn‖I/NC is 0.4 V larger than the Zn‖I/Co_9S_8@NC battery (Figure S31, Supporting Information). The lower polarization voltage at low temperatures can be attributed to the catalytic and structural advantages of the Co_9S_8@NC electrode. Moreover, the capacity retention was 90.16% of ultrahigh as 376 mAh g^{-1} based on the Zn‖I/Co_9S_8@NC at −30 °C after 200 cycles at 1 A g^{-1} (Figure 6c). At a high current density of 5 A g^{-1}, it exhibited a stable cycling performance of 2000 cycles without apparent capacity degradation and an average reversible capacity of 315 mAh g^{-1} (Figure 6d). Taken together, compared with the generally applied carbon host materials, the Co_9S_8@NC might accommodate a higher power density at relatively high working currents due to the improved reaction kinetics. Moreover, the electrochemical performance at low temperatures might be another advantage of our Co_9S_8@NC due to the reduced activation energy for the conversion reactions for the iodine electrode.

Additionally, a large soft pack of Zn‖I/Co_9S_8@NC battery with the size of 3 cm × 4 cm was further performed to demonstrate its potential for practical applications (Figure 6e). At room temperature, the capacity retention rate was 86.67%, with a reversible capacity of 365 mAh g^{-1}, after 100 cycles at 1 A g^{-1}. However, the capacity retention rate was notably higher as 97.25% at low temperatures after 100 cycles, where the average reversible capacity at low temperatures was 354 mAh g^{-1} (Figure 6f).

3. Conclusions

To fully exploit the cascade iodine electrode chemistry by utilizing the two-electron transfer reaction, we have developed an efficient catalyst to catalytically improve the energy density and power density. Conducive catalytic configurations were constructed based on the high specific surface area of honeycomb interconnected nanochannels and the monodisperse Co_9S_8 onto the NC supporting frameworks. Of much interest is, the charge-deficient Co_9S_8@NC was configured to promote the strong chemisorption effect of the active iodine species and promote the charge transfer kinetics with the cascading two-electron transfer reaction, i.e., $I^+/I^0/I^-$, at both normal and low temperatures. As a result, the energy density and power density of the battery were significantly improved. Our Zn‖I/Co_9S_8@NC battery exhibits a high energy density of 554 Wh kg^{-1}, high power density of 1526 W kg^{-1}, and excellent cycling stability of 5000 cycles at a high current of 5 A g^{-1} at a normal temperature of 30 °C. Moreover, at a low temperature of −30 °C, it could deliver an energy of 485 Wh kg^{-1}, a power of 1514 W kg^{-1}, and ultrastable cycling performance. The as-delivered performance enabled our $I^+/I^0/I^-$ electrode as a competitive electrode candidate among the generally applied cathode electrodes for Zn-based battery systems. This work offers new insights by catalytically regulating the conversion electrodes for aqueous Zn-based battery chemistry, such as the halogen and chalcogen electrode chemistry, obtaining high-energy and high-power battery systems.

Supporting Information

Supporting Information is available from the Wiley Online Library or from the author.

Acknowledgements

T.H., and Y.Z. contributed equally to this work. This research was supported by the National Key R&D Program of China under Project No. 2019YFA0705104, Excellent Youth Fund of Anhui Province (No. 2108085Y17), Innovation and Entrepreneurship Support Plan of Anhui Province for Returned Personnels Studying Abroad (No. 2022LCX001), and Hundred-Talent Program of Anhui Province. The work was also partially sponsored by GRFs under Project CityU 11304921. The authors also gratefully acknowledged the financial support by Shenzhen Municipality under Stability Support Program of Shenzhen Colleges and Universities (Grant No. GXWD20220817150352006), Shenzhen Science and Technology Program (Grant No. RCBS20221008093222009), Project of Scientific Research Foundation for Returned Scholars (Grant No. DD11409018), and State Key Laboratory of New Textile Materials and Advanced Processing Technologies (No. FZ20230010).

Conflict of Interest

The authors declare no conflict of interest.

Data Availability Statement

The data that support the findings of this study are available from the corresponding author upon reasonable request.

Keywords

cascade conversion reaction, charge-deficient catalyst, high energy and power battery, low-working temperature battery, two-electron transfer iodine electrode

Received: November 16, 2023
Revised: December 21, 2023
Published online: February 1, 2024

[1] R. C. Massé, C. Liu, Y. Li, L. Mai, G. Cao, *Natl. Sci. Rev.* **2017**, *4*, 26.
[2] Z. Cao, G. Liang, D. Ho, C. Zhi, H. Hu, *Adv. Funct. Mater.* **2023**, *33*, 2303060.
[3] C. Bai, F. Cai, L. Wang, S. Guo, X. Liu, Z. Yuan, *Nano Res.* **2018**, *11*, 3548.
[4] Y. Zou, T. Liu, Q. Du, Y. Li, H. Yi, X. Zhou, Z. Li, L. Gao, L. Zhang, X. Liang, *Nat. Commun.* **2021**, *12*, 170.
[5] H. Yu, Z. Wang, R. Zheng, L. Yan, L. Zhang, J. Shu, *Angew. Chem., Int. Ed.* **2023**, *62*, 202308397.
[6] X. Li, M. Li, Z. Huang, G. Liang, Ze Chen, Qi Yang, Q. Huang, C. Zhi, *Energy Environ. Sci.* **2021**, *14*, 407.
[7] G. Liang, B. Liang, A. Chen, J. Zhu, Q. Li, Z. Huang, X. Li, Y. Wang, X. Wang, B. Xiong, X. Jin, S. Bai, J. Fan, C. Zhi, *Nat. Commun.* **2023**, *14*, 1856.
[8] C. Liu, Z. G. Neale, G. Cao, *Mater. Today* **2016**, *19*, 109.
[9] L. Peng, Z. Wei, C. Wan, J. Li, Z. Chen, D. Zhu, D. Baumann, H. Liu, C. S. Allen, X. Xu, A. I. Kirkland, I. Shakir, Z. Almutairi, S. Tolbert, B. Dunn, Y Huang, P. Sautet, X. Duan, *Nat. Catal.* **2020**, *3*, 762.
[10] W. Gao, S. Cheng, Y. Zhang, E. Xie, J. Fu, *Adv. Funct. Mater.* **2023**, *33*, 2211979.
[11] M. Liu, Q. Chen, X. Cao, D. Tan, J. Ma, J. Zhang, *J. Am. Chem. Soc.* **2022**, *144*, 21683.
[12] T. Liu, H. Wang, C. Lei, Y. Mao, H. Wang, X. He, X. Liang, *Energy Storage Mater.* **2022**, *53*, 544.
[13] L. M. Y. Ying, S. Chen, Z. Huang, X. Li, H. Huang, C. Zhi, *Angew. Chem. Int. Ed.* **2021**, *60*, 3791.
[14] X. Lu, D. Wang, L. Ge, L. Xiao, H. Zhang, L. Liu, J. Zhang, M. An, P. Yang, *New J. Chem.* **2018**, *42*, 19665.
[15] S. Chen, Q. Chen, S. Ding, Y. Tian, J. Wang, S. Hou, J. Zhang, *Nano Res.* **2023**, *16*, 4246.
[16] Z.-Q. Cao, M. Z. Wu, H.-B. Hu, G. J. Liang, C. Y. Zhi, *NPG Asia Mater* **2018**, *10*, 670.
[17] J. Wang, Q. Wei, Q. Ma, Z. Guo, F. Qin, Z. R. Ismagilov, W. Shen, *Appl. Catal., B* **2020**, *263*, 118339.
[18] G. Liang, J. Zhu, B. Yan, Q. Li, A. Chen, Z. Chen, X. Wang, B. Xiong, J. Fan, J. Xu, C. Zhi, *Energy Environ. Sci.* **2022**, *15*, 1086.
[19] Y. Wu, N. He, G. Liang, C. Zhang, C. Liang, D. Ho, M. Wu, H. Hu, *Adv. Funct. Mater.* **2023**, 2301734. https://orcid.org/10.1002/adfm.202301734
[20] L. Jiao, G. Wan, R. Zhang, H. Zhou, S. H. Yu, H. L. Jiang, *Angew. Chem., Int. Ed.* **2018**, *130*, 8661.
[21] Y. He, M. Liu, S. Chen, J. Zhang, *Sci. China Chem* **2022**, *65*, 391.
[22] S. Xue, J. Shang, X. Pu, H. Cheng, L. Zhang, C. Wang, C.-S. Lee, Y. Tang, *Energy Storage Mater.* **2023**, *55*, 33.
[23] B. Qiu, L. Cai, Y. Wang, X. Guo, S. Ma, Ye Zhu, Y. H. Tsang, Z. Zheng, R. Zheng, Y. Chai, *Small* **2019**, *15*, 1904507.
[24] Y. Hou, X. Du, S. Scheiner, D. P. Mcmeekin, Z. Wang, N. Li, M. S. Killian, H. Chen, M. Richter, I. Levchuk, N. Schrenker, E. Spiecker, T. Stubhan, N. A. Luechinger, A. Hirsch, P. Schmuki, H.-P. Steinrück, R. H. Fink, M. Halik, H. J. Snaith, C. J. Brabec, *Science* **2017**, *358*, 1192.
[25] W. Xu, W. Tian, L. Meng, F. Cao, L. Li, *Adv. Energy Mater.* **2021**, *11*, 2003500.
[26] Y. Tian, Z. Wu, M. Li, Q. Sun, H. Chen, D. Yuan, D. Deng, B. Johannessen, Y. Wang, Y. Zhong, Li Xu, J. Lu, S. Zhang, *Adv. Funct. Mater.* **2022**, *32*, 2209273.
[27] Y. Lu, C.-Z. Zhao, J.-Q. Huang, Q. Zhang, *Joule* **2022**, *6*, 1172.
[28] C. Sheng, F. Yu, C. Li, H. Zhang, J. Huang, Y. Wu, M. Armand, Y. Chen, *J. Phys. Chem. Lett.* **2021**, *12*, 2064.
[29] Y. Niu, Y. Zhou, W. Zhang, Y. Zhang, C. Evans, Z. Luo, N. Kane, Y. Ding, Y. Chen, X. Guo, W. Lv, M. Liu, *Adv. Energy Mater.* **2022**, *12*, 2103783.
[30] X. Li, Y. Wang, Z. Chen, P. Li, G. Liang, Z. Huang, Q. Yang, A. Chen, H. Cui, B. Dong, H. He, C. Zhi, *Angew. Chem., Int. Ed.* **2022**, *61*, 202113576.
[31] Y. Du, R. Kang, H. Jin, W. Zhou, W. Zhang, H. Wang, J. Qin, J. Wan, G. Chen, J. Zhang, *Adv. Funct. Mater.* **2023**, *33*, 2304811.
[32] H. Pan, Y. Shao, P. Yan, Y. Cheng, K. S. Han, Z. Nie, C. Wang, J. Yang, X. Li, P. Bhattacharya, K. T. Mueller, J. Liu, *Nat. Energy* **2016**, *1*, 16039.
[33] K. W. Nam, S. S. Park, R. dos Reis, V. P. Dravid, H. Kim, C. A. Mirkin, J. F. Stoddart, *Nat. Commun.* **2019**, *10*, 4948.
[34] D. Kundu, B. D. Adams, V. Duffort, S. H. Vajargah, L. F. Nazar, *Nat. Energy* **2016**, *1*, 16119.
[35] Y. Li, L. Liu, H. Li, F. Cheng, J. Chen, *ChemComm* **2018**, *54*, 6792.
[36] C. Xia, J. Guo, Y. Lei, H. Liang, C. Zhao, H. N. Alshareef, *Adv. Mater.* **2018**, *30*, 1705580.
[37] L. Zhang, L. Chen, X. Zhou, Z. Liu, *Adv. Energy Mater.* **2015**, *5*, 1400930.
[38] W. Li, H. Xu, H. Zhang, F. Wei, T. Zhang, Y. Wu, L. Huang, J. Fu, C. Jing, J. Cheng, S Liu, *Energy Environ. Sci.* **2023**,*16*, 4502.